Deterioration of form accuracy induced by servo dynamics errors and real-time compensation for slow tool servo diamond turning of complex-shaped optics

Abstract

Tool servo diamond turning is a promising method for generating complex-shaped optics. Considering the dynamic oscillation of the tool, servo dynamics are essential for the accuracy of the form generated with tool servo turning. Although static geometric errors and multiple compensation strategies for these errors have been studied extensively, the effects of dynamics errors of the servo axis on surface quality have received less attention. In this study, a dynamic surface generation model is established by considering the coupling effect between the servo axis dynamics and the cutting force. Using a micro-lens array (MLA) as an example, the components of the servo dynamics error of the servo motion, including dynamic deformation, resonant vibration, and trajectory tracking error, are characterised. The relationship between the servo dynamics error and the resulting form error is then theoretically identified with experimental verification. To compensate for the servo dynamics error in real-time, the concept of a cooperative tool servo (CTS) is proposed by incorporating a slow tool servo (STS) into a fast tool servo using a master-slave control strategy. Relative to using a STS for turning an MLA, the peak-to-valley (PV) servo motion error when using a CTS decreases from 4.8 μm to 0.3 μm experimentally, and the corresponding PV form error for one hexagonal lenslet decreases from 4 μm to 1.4 μm, demonstrating the effectiveness and superiority of a CTS for dynamics error compensation in the manufacturing of complex-shaped optics.

Keywords: Ultra-precision diamond turning, servo dynamic error, micro-structured optics, cooperative tool servo

1. Introduction

Tool servo diamond turning that includes a slow tool servo (STS) or a fast tool servo (FTS) is a promising approach for generating complex-shaped optics with ultra-precision because of the auxiliary oscillation provided by the servo axis [1]. Form accuracy during turning is a critical issue in optics manufacturing. The effects of static geometric errors on form accuracy have been comprehensively studied in freeform and micro-structured surface generation, considering the geometric motion of the machine tool and geometric machining parameters. Static error sources in tool servo turning that have been identified to date include multi-directional error motions of the linear moving axes [2, 3], spindle rotation errors [4], tool alignment errors [5], tool nose geometry [6], and toolpath sampling intervals [7]. To compensate for these static errors, error model-based toolpath modifications [2, 6, 8] and closed-loop manufacturing, which repeats the cutting, measurement, and compensation procedures [9–11], have been proposed.

In addition to static geometric errors, servo dynamics error plays a key role in the surface quality of forms generated with tool servo turning, especially considering the dynamic nature of the oscillation of the tool. In this study, servo dynamics error is defined as the frequency-dependent error of the servo axis induced by external disturbances and by the system itself. In general, servo dynamics error consists of the dynamic deformation induced by position-dependent cutting forces, resonant vibration, and the trajectory tracking error induced by the frequency-dependent amplitude variation and phase-lag effects of the servo axis. Among these three primary sources, the force-induced dynamic deformation is strongly coupled with the other two dynamic factors, and its contribution is challenging to identify in experiments. Currently, there is a focus on the resonant vibration of the servo system because the induced vibration marks affect the roughness of the machined surface, particularly when turning certain discontinuously structured surfaces. For example, vibration marks have been frequently observed on the surfaces of micro-lens arrays (MLAs) generated with tool servo turning [12, 13].

To suppress resonant vibrations when turning MLAs, cutting velocity adjustments, acceleration restrictions [13, 14], and segmented turning approaches to toolpath smoothing have been proposed [15, 16]. In general, adjusting the cutting velocity through the quasi-elliptical tool motion requires another oscillation along the cutting direction; such adjustments increase equipment cost and introduce additional motion error [14]. Slowing the cutting velocity and segmenting the MLA are simple and effective approaches, but they decrease the machining efficiency [13, 16]. Moreover, segmented turning does not provide a fundamental solution for different surface shapes, and tra-

jectory tracking errors are observed that are not compensated for by segmented turning [16].

Although the effect of trajectory tracking errors on surface generation has not been extensively studied, a pioneering study that attempted to compensate for frequency-dependent amplitude variation and phase-lag effects was conducted for FTS turning [3]. As was done for static geometric errors, pre-shaping the tool trajectory was proposed as a dynamic compensation approach. By inverting the system dynamics using a first-order system approximation, a compensation tool trajectory was derived [3]. However, such a compensation strategy is a static process that does not consider factors that vary over time in practical turning operations. Therefore, an effective solution will be restricted to repeatable turning; for example, fluctuations of spindle speed that decrease accuracy improvement will not be considered.

In general, the most direct solution to minimise tracking error is to improve the control strategy by tuning control parameters to specific cutting conditions [8]. A control system frequently used in FTS and STS operations is the proportional-integral-derivative (PID)-based controller [16, 17]. Ametek Precitech employed an adaptive state feedback approach to improve the control performance of STS, enhance tracking accuracy, and increase system robustness [17]. The aim of this effort was to develop advanced control strategies for FTS that considered the nonlinearity of the system and external disturbances. Methods that effectively improved system performance included sliding mode-based [3, 18], active disturbance rejection-based [19], and repetitive control [9, 20]. Among these strategies, the repetitive control-based method was the best approach for high-frequency tracking with ultra-high accuracy. However, repetitive control methods can only handle periodic commands, and a slight deviation from the specified periodicity may cause the control performance to deteriorate or become ineffective [20]. Moreover, regardless of the strategy adopted, tracking accuracy is constrained by properties that are inherent to the drive systems; therefore, even adopting advanced control strategies can result in small improvements. For these reasons, more advanced compensation methods are required in addition to improving control performance.

In summary, current understanding of the effects of servo dynamics errors on the form accuracy of complex-shaped optical surfaces is limited. Although some pioneering studies have proposed strategies to compensate for servo dynamics errors, these strategies focus on one aspect; therefore, the inherent conflict between the static nature of the application of these strategies and the variable nature of servo dynamics errors over time significantly restricts the flexibility and applicability of these compensation operations.

To address the issues discussed above, in this study, a systematic investigation of the effect of servo dynamics errors on the generation of complicated surfaces by numerical simulation and experimental verification was conducted. The dynamics of a typical slow tool servo (STS) system are modelled and identified in practice, and the relationship between the servo dynamics errors and the accuracy of the generated form is characterised in detail. Furthermore, instead of using static error compensation approaches, the concept of cooperative tool servo (CTS) is proposed and experimentally demonstrated to be a generally applicable and robust strategy for real-time compensation of servo dynamics errors.

2. Dynamics of an STS

The approach to modelling the dynamics of the response of the STS slide motion to external disturbances has been to consider the response as a second-order system with one degree-of-freedom (DoF). However, such an approach is not applicable to the z-axis of the servo trajectory [21, 22]. To consider the driving system, a detailed dynamics model was established that considers the mechatronic driving system and control algorithm [23]. To use this model, detailed knowledge of each component in the machine is required, and the external cutting force is superimposed onto the driving force, which is not the case in practice [23]. Therefore, to overcome these limitations, we developed an equivalent 2-DoF dynamics model to simultaneously consider the desired command and the external force.

2.1. Dynamics modeling

A photograph of the servo axis with a closed-loop slide and an open-loop slide tool coupling system is shown in Fig. 1(a), and the equivalent dynamics model is presented in Fig. 1(b). Assuming the spring-mass-damping structure of the closed-loop slide from the viewpoint of the output port, the resulting response related to the force acting on the sliding table can be described as a second-order differential system. In addition, the mechanical structure of the coupled slide tools can also be simplified as a second-order system with a lumped mass of m_t [24].

Assuming that $z_t(t)$ and $z_s(t)$ are the motions of the tool and slide, the governing equation for the servo axis dynamics can be obtained as follows [24]:

$$\begin{bmatrix} m_t & 0 \\ 0 & m_s \end{bmatrix} \begin{bmatrix} \ddot{z}_t(t) \\ \ddot{z}_s(t) \end{bmatrix} + \begin{bmatrix} c_t & -c_t \\ -c_t & c_t + c_s \end{bmatrix} \begin{bmatrix} \dot{z}_t(t) \\ \dot{z}_s(t) \end{bmatrix} + \begin{bmatrix} k_t & -k_t \\ -k_t & k_t + k_s \end{bmatrix} \begin{bmatrix} z_t(t) \\ z_s(t) \end{bmatrix} = \begin{bmatrix} -f_t(t) \\ f_a(t) \end{bmatrix}, \tag{1}$$

where $f_t(t)$ and $f_a(t)$ denote the thrust of the cutting force on the tool and the equivalent driving force on the sliding table, respectively.

By setting the external force to zero($F_t(t) = 0$), the transfer function relating the tool motion $z_t(t)$ and the slide motion $z_s(t)$ can be derived by performing the

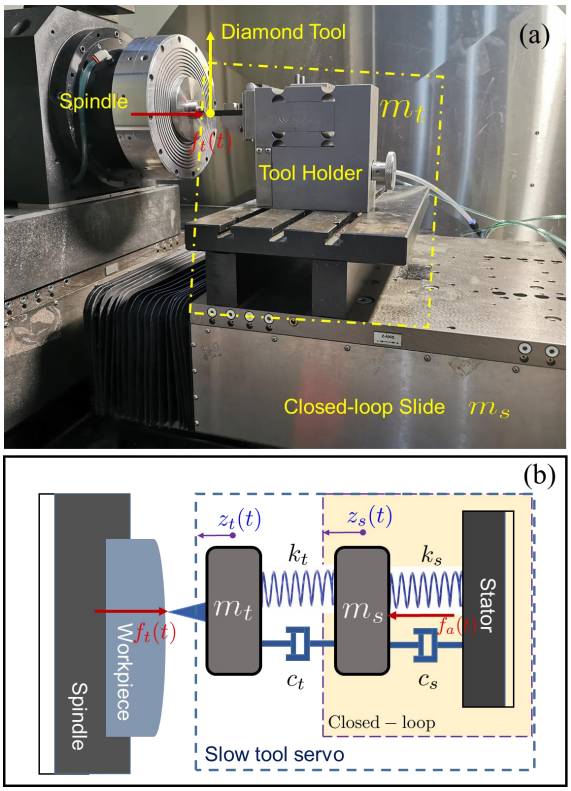

Figure 1: The servo axis of a typical STS system. (a) A photograph, and (b) the equivalent servo dynamics model, where m_t is the lumped moving mass of the tool, c_t and k_t are the equivalent damping ratio and stiffness of the slide-tool coupling system, respectively, and m_s, c_s, and k_s are the equivalent moving mass, damping ratio, and output stiffness of the slide.

Laplace transformation of Eq. 1 as

$$G_s(s) = \frac{Z_t(s)}{Z_s(s)} = \frac{c_t s + k_t}{m_t s^2 + c_t s + k_t} = \frac{2\xi_t \omega_t s + \omega_t^2}{s^2 + 2\xi_t \omega_t s + \omega_t^2}, \tag{2}$$

where s is the Laplace operator, $\omega_t = \sqrt{\frac{k_t}{m_t}}$, $\xi_t = \sqrt{\frac{m_t}{k_t}} \cdot \frac{c_t}{2}$, $Z_t(s) = \mathcal{L}[z_t(t)]$, and $F_a(s) = \mathcal{L}[f_a(t)]$, with $\mathcal{L}(\cdot)$ representing the operation for Laplace transformation.

Without loss of generality, the transfer function relating the desired command $z_d(t)$ and the slide motion $z_s(t)$ in the closed-loop mode can be expressed by

$$G_d(s) = \frac{Z_s(s)}{Z_d(s)} = \frac{\sum_{l=1}^{\mathrm{L}} b_l s^l}{\sum_{k=1}^{\mathrm{K}} a_k s^k}, \ \mathrm{K} - \mathrm{L} \geq 0, \tag{3}$$

where b_l and a_k are the constants to be identified from the practical response. The response of the toolpath in the spatial domain to the desired command for the machine tool in the time domain is detailed in Appendix A.

By ignoring the actuation force, the transfer function relating the tool motion $z_t(t)$ and the external cutting force $f_t(t)$ can be derived from Eq. 1 as

$$\begin{aligned} G_f(s) &= \frac{Z_t(s)}{F_t(s)} \\ &= -\frac{\Delta(s) + c_t s + k_t}{(m_t s^2 + c_t s + k_t) \cdot \Delta(s) + m_t s^2 (c_t s + k_t)} \end{aligned}, \tag{4}$$

where $\Delta(s) = m_s s^2 + c_s s + k_s$, and $F_t(s) = \mathcal{L}[f_t(t)]$. Furthermore, this equation can be simplified to

$$G_f(s) = \frac{Z_t(s)}{F_t(s)} = \frac{-P(s) - G_s(s)}{m_t \left[s^2 G_s(s) + \beta s^2 + 2\beta\alpha_m \xi_t \omega_t s + \alpha_m^2 \omega_t^2\right]}, \tag{5}$$

with

$$P(s) = \frac{\Delta(s)}{m_t s^2 + c_t s + k_t} = \frac{\beta s^2 + 2\beta\alpha_m \xi_s \omega_t s + \alpha_m^2 \omega_t^2}{s^2 + 2\xi_t \omega_t s + \omega_t^2}, \tag{6}$$

where $\beta = \frac{m_s}{m_t}$ and $\alpha_m = \sqrt{\frac{k_s}{k_t}}$ are the constant mass ratio and stiffness ratio, respectively.

In general, the stiffness and the natural frequency of the slide-tool coupling joint are designed to be much higher than the working frequency to avoid undesired vibrations. Therefore, for a given working condition with frequency $\omega \ll \omega_t$, the transfer function of $G_s(s)$ can be simplified by setting $\left(\frac{\omega}{\omega_t}\right)^2 \approx 0$ as follows:

$$G_s(s)|_{s=j\omega} = G_s(j\omega) = \frac{2\xi_t \frac{j\omega}{\omega_t} + 1}{-\left(\frac{\omega}{\omega_t}\right)^2 + 2\xi_t \frac{j\omega}{\omega_t} + 1} \approx 1, \tag{7}$$

where $j^2 = -1$.

Similarly, the transfer function of $G_f(s)$ can be simplified as a second-order system as follows:

$$G_f(s) \approx \frac{-\left(1 + \alpha_m^2\right)}{m_t \left[(1+\beta) s^2 + 2\beta\alpha_m \xi_s \omega_t s + \alpha_m^2 \omega_t^2\right]}. \tag{8}$$

Therefore, the final tool motion that is subjected to the desired trajectory and the external cutting force can be obtained in the frequency domain as

$$\begin{aligned} Z_t(s) &= G_d(s) G_s(s) X_d(s) + G_f(s) F_t(s) \\ &\approx G_d(s) X_d(s) + G_f(s) F_t(s) \end{aligned}. \tag{9}$$

Note 1. Considering the mass damper structure of the linear direct-drive motor [23, 24], the input stiffness can be neglected from the viewpoint of the driving port. However, an output stiffness k_s, which is equivalent to the force on the sliding table, may exist due to the disturbance rejection capability of the closed-loop system, and the stiffness value might be highly dependent on the performance of the control algorithm.

Note 2. The actuation force $f_a(t)$ is equivalent to the driving force on the sliding table required to achieve the motion $x_s(t)$. Because the transfer function relating the com-

manded motion $x_d(t)$ to the actual motion $x_s(t)$ is identified from the practical response, modelling of the complex relationship inside the driving and control systems is unnecessary, which simplifies the modelling process.

Note 3. When the working frequency ω is much smaller than ω_t, the transfer function can be simplified to $G_f(s) = \left(1 + \frac{1}{\alpha_m^2}\right) \cdot \frac{1}{m_t \omega_t^2}$. Therefore:

a) If $k_s \ll k_t$ ($\alpha_m \to 0$), then $G_f(s) \to \frac{1}{m_t \omega_t^2 \alpha_m^2} = \frac{1}{k_s}$. The primary cause of a deformation subjected to an external force will be the sliding system.

b) If $k_s \gg k_t$ ($\alpha_m \to \infty$), then $G_f(s) \to \frac{1}{m_t \omega_t^2} = \frac{1}{k_t}$. The primary cause of the deformation will be the slide-tool coupling system.

2.2. Practical dynamics characteristics

2.2.1. System dynamics identification

A commercial ultra-precision machine tool (450UPL, Moore Nanotech, USA) with three controlled axes (XZC), as shown in Fig. 1(a) was used for the experimental investigation. To identify the dynamics behavior, step response testing is conducted using a 5 μm step command, and the practical motion of the servo axis is recorded through an externally attached linear grating with a resolution of 1 nm (Renishaw, UK). The desired command and practical step response are illustrated in Fig. 2(a), which shows an overshoot at approximately 36.8%. By conducting the system identification in the time domain, the equivalent transfer function $G_d(s)$ in Eq. 3 can be identified as

$$G_d(s) = \frac{\left(\begin{array}{l} 9.89 \times 10^7 s^3 + 8.62 \times 10^{10} s^2 \\ +1.70 \times 10^{13} s + 1.58 \times 10^{15} \end{array}\right)}{\left(\begin{array}{l} s^6 + 1142 s^5 + 1.01 \times 10^6 s^4 + 4.42 \times 10^8 s^3 \\ +1.36 \times 10^{11} s^2 + 2.12 \times 10^{13} s + 1.58 \times 10^{15} \end{array}\right)} \tag{10}$$

Overall, the estimated step response in Fig. 2(a) exhibits a good agreement with the practical response, suggesting that the dynamics behaviour of the STS system is accurately described by the proposed system model. The Bode diagram of $G_d(s)$ is presented in Fig. 2(b) to illustrate the dynamics behaviour of the STS system in the frequency domain. The resonant frequency is approximately 53 Hz, with a resonant peak of 4 dB (58%). As for the phase-frequency function, the phase lags are approximately 8 deg and 17 deg for the working frequencies of 10 and 20 Hz, respectively.

2.2.2. Servo dynamics errors

To directly investigate the dynamic behaviour of trajectory tracking errors of the servo axis, the frequency responses of the tracking errors $E_s(s) = 1 - G_d(s)$ are also shown in Fig. 2(b). Frequency responses are jointly determined by the amplitude variation and phase-lag effects of $G_d(s)$. The amplitude of the errors related to the entire bandwidth shown in Fig. 2(b)increases when the frequency of the trajectory increases before the resonant point. For instance, the error amplitudes are approximately1.78% (-35 dB) and 14% (-17 dB) of the desired motion at working frequencies of 1 Hz and 10 Hz, respectively.

These results demonstrate that high-frequency tracking may lead to a large tracking error. Because the typical trajectory in STS turning is constructed by the sum of the harmonics of the spindle revolution [20], a low spindle speed is required to decrease the component frequencies of the trajectory. Although this may lead to small tracking error, the machining time might be greatly increased. Therefore, to have a sufficient machining efficiency, the spindle speed needs to be maximized with the constraint of an acceptable tracking error.

3. Modeling of the dynamic surface generation

As reported, there are a variety of nonlinear factors involved in surface generation [23, 25]. Because a primary factor may contribute more to surface roughness, a simplified model that considers the shearing and ploughing

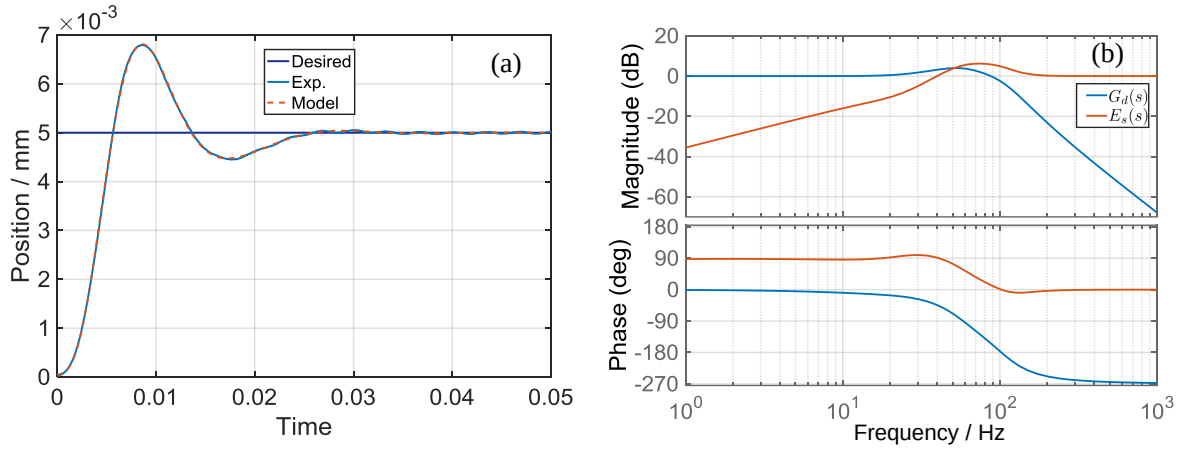

Figure 2: Dynamics response of the STS diamond turning system. (a) The step response; (b) the dynamics in the frequency domain.

effects of the interaction between the tool and the work material is established. The effects of the rake angle, friction, and material properties are combined into one specific force coefficient; this approach is commonly adopted in metal cutting [26–28].

3.1. Simplified cutting force model

To simplify the model, the cutting force induced by shear flow is approximately proportional to the effective cutting area S_c; therefore, the thrust force $f_{t,s}$ for a given cutter location position (CLP) can be expressed as follows [27, 28]:

$$f_{t,s} = \lambda S_c + f_o, \tag{11}$$

where λ is the specific force coefficient relating the material removal area S_c to the thrust force, and f_o is assumed to be a constant force bias determined by the material and tool geometry [27]. The material removal area S_c is highly dependent on the current CLP and the corresponding CLP from the previous revolution, which is detailed in Appendix B.

With respect to diamond turning, a ploughing effect occurs when the practical depth-of-cut is smaller than a minimum one [29, 30]. To avoid tool edge discretization, a saturation function is employed to approximate the ploughing effect on a minimum area δ_s. Considering the continuous nature of the process, the force $f_t(t)$ can be described by

$$f_t = \begin{cases} f_{t,s}, & S_c \in [\delta_s, +\infty) \\ \left(\lambda + \frac{f_o}{\Delta_s}\right) \cdot S_c, & S_c \in (0, \delta_s) \\ 0, & S_c \in (-\infty, 0] \end{cases} \tag{12}$$

3.2. Surface generation model

The coupling relationship between the desired command and the tool motion subjected to external cutting forces is illustrated in Fig. 3. By constructing a corresponding block model in the MATLAB/Simulink modulus, the motion $z_t(t)$ can be easily solved using the fourth Runge-Kutta algorithm. Without loss of generality, the spindle speed is assumed to be constant in this study. Therefore, by referring to section Appendix A, the delayed time τ for the model can be easily determined by $\tau = \frac{60}{n}$. If the spindle speed is time-varying, the delayed time τ needs to be adjusted to satisfy $\theta(t) - \theta(t-\tau) \equiv 2\pi$.

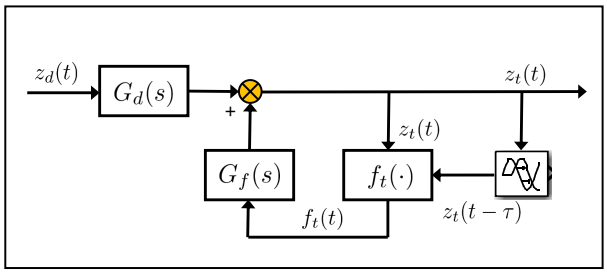

Figure 3: Schematic of the coupled model for tool motion in the STS, where $f_t(\cdot)$ is the nonlinear function of the cutting force.

To estimate the generated surface, the tool motion $z_t(t)$ can then be re-mapped to the coordinate system of the workpiece as $z_{k,l}^{(s)}$ by means of Eq. A.1 and Eq. A.2. Moreover, a uniform surface meshing method in the cylindrical coordinate system is employed to simplify the calculation process and decrease the computational effort; namely, $S = (\rho_s, \theta_s, s_z)$. Considering the relative position between the CLPs $o_{k,l}$ and $o_{k-1,l}$, the equation to estimate the generated surface can be expressed as

$$s_z = \begin{cases} s_n, & S_c \in (\Delta_s, \infty) \\ (1-\epsilon_p)\,(s_n - s_z)\,, & S_c \in (0, \Delta_s) \\ s_z, & S_c \in (-\infty, 0] \end{cases} \tag{13}$$

where ϵ_p is a material dependent coefficient for the rough description of the ploughing-induced elastic recovery effect [30], and s_n is the new surface determined by [30].

$$s_n = \sqrt{r_\epsilon^2 - (\rho_s - \rho_{k,l})^2} + z_{k,l}^{(s)},\ \forall \rho_s \in [\rho_{k,l} + x_a, \rho_{k,l} + x_c] \tag{14}$$

Taking $x_s = \rho_s \cos\theta_s$ and $y_s = \rho_s \sin\theta_s$, the estimated surface can be transferred to the Cartesian coordinate system $S = (x_s, y_s, s_z)$, and a uniformly described surface in the system $S = (x_s, y_s, s_z)$ can be estimated through a three-dimensional (3D) spline-based interpolation.

4. Numerical simulation and discussion

A typical hexagonal spherical MLA is adopted as the example for simulating the tool servo turning. The overall aperture of the simulated surface is 10 mm, and the circumscribed diameter and height of each spherical lenslet are 1 mm and 50 μm, respectively. The nose radius of the diamond tool with zero rake angle is set as r_ϵ = 1 mm, and the feedrate is set as f_r =40 μm/rev. The practically identified system transfer function $G_a(s)$ is employed for the simulation, and $\xi_s = 0.7$ is employed for estimating the responses of the tool to external disturbances. The equivalent stiffness of the slide used to measure the external force rejection is estimated as $k_s = 200$ N/μm. Since sufficiently high stiffness is normally required for the slide-tool coupling system, its stiffness is also estimated as $k_t = 200$ N/μm ($\alpha_m = 1$), and the frequency is $\omega_t = \sqrt{\frac{k_t}{m_t}}$, with $m_t = 5$ kg. Considering the volume of the solid part of the slide table is about twice of the tool holder, the mass coefficient is then estimated as $\beta = \frac{m_s}{m_t} = 2$.

By considering the reported result as a conventional milling of easy-to-cut metallic alloys [27, 31] as well as our previous cutting experiments [29], the force coefficient is estimated to be λ =1000 N/mm^2. In general, the coefficient λ is a process-dependent factor that varies with respect to material property, cutting velocity, tool shape, tool state, and lubricant conditions [31, 32]. In the established system dynamics model, the relationship between the coefficient and force is linear; therefore, variation in the specific force coefficient may lead to linear variation

in the amplitude of the dynamic deformation and a slight change in the final tracking error.

4.1. Simulated servo motions

The power spectrum density of the resulting toolpath is illustrated in Fig. 4. Due to the nature of hexagonal arrangement of the MLA, the fundamental frequency of the toolpath is observed to be approximately six times ω_o, and a set of components with multiple frequencies are further superimposed as shown in Fig. 4. In general, the number of frequency components and the highest frequency are determined by the size of the lenslet relative to the overall aperture of the MLA.

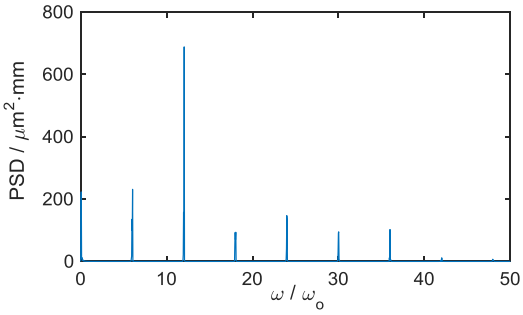

Figure 4: The power spectrum density (PSD) of the simulated toolpath with respect to the relative frequency (ω) normalised to the spindle frequency (ω_o).

By solving the feedback model in Fig. 3, the simulated tool motions with spindle speeds of $n = 30$ rpm and $n = 15$ rpm are compared in Fig. 5(a) and Fig. 5(c), respectively, together with the desired command. Compared with the desired command, a better motion agreement is observed with the slower spindle speed of $n = 15$ rpm. Resonant vibration induces a large deviation between the desired and simulated motion at sharp points that have large accelerations. With respect to the servo motion errors shown in Fig. 5(b) and Fig. 5(d), the peak-to-valley (PV) tracking errors, which include the resonant vibration errors, are approximately 16.5 μm and 7.6 μm for the two cases; these errors are approximately 33% and 15.2% of the full-motion span of the desired command.

As discussed above, to achieve an acceptable tracking error, sufficiently low spindle speed is required to decrease the motion frequency. For example, using a spindle speed of n =1 rpm, the PV error can be reduced to approximately 1 μm for the same command segment shown in Fig. 5. However, a 1 μm error is still too large for ultra-precision turning.

4.2. Simulated dynamic deformation

The dynamic deformation $d_z = G_f(s)F_t(s)$ with spindle speeds of 15 rpm and 30 rpm is presented in Fig. 6, where the trajectory segment is the same as that shown in Fig. 5(a) and (c). The time axis is normalised from 0 to 1 to better compare the basic features of the dynamic deformation at different cutting speeds.

As shown in Fig. 6, the maximum deformation is approximately 35 nm, and the deformation shape is notably different from that of the tool trajectory. This difference may be because the cutting force is dependent on not only the current CLP but also the corresponding CLP during the previous revolution. Although the two dynamic deformations share similar features, the vibration that occurs at a higher spindle speed (n = 30 rpm) is larger. The servo axis dynamics and the instantaneous cutting force,

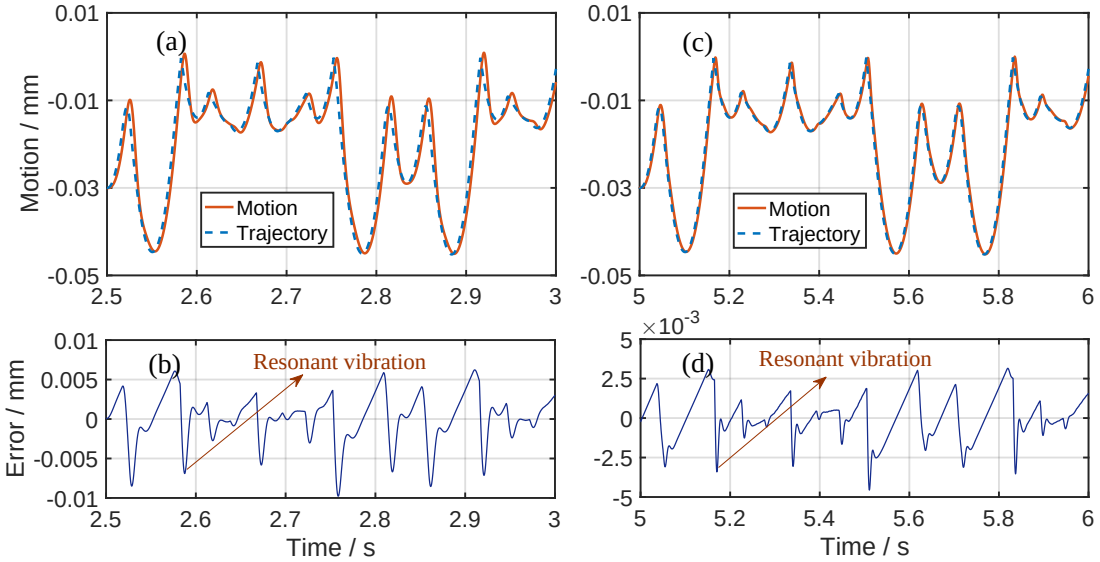

Figure 5: The estimated servo motion with spindle speeds of (a) 30 rpm and (c) 15 rpm, and the servo motion error with spindle speeds of (b) 30 rpm and (d) 15 rpm.

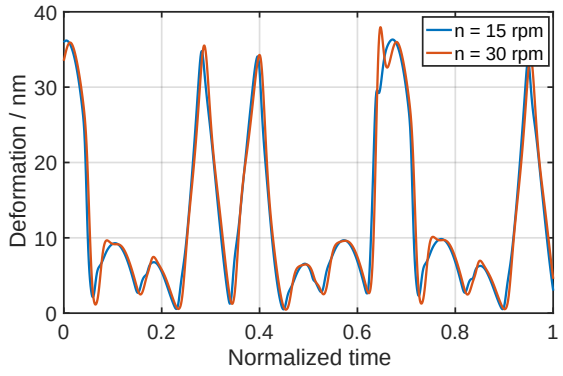

Figure 6: The coupled dynamic deformation of the tool induced by external cutting forces.

which is strongly coupled to the desired command, both contribute to the dynamic deformation.

In general, the dynamic deformation induced by the cutting force is much smaller than the trajectory tracking error. However, considering the required form accuracy for ultra-precision machining, dynamic deformation error might need to be considered.

4.3. Simulated surface generation

4.3.1. Form error distribution

Considering the coupled dynamics, the generated surface is numerically simulated with a spindle speed of $n = 30$ rpm. The surface that is generated over a large area is projected on the XY plane, as illustrated in Fig. 7(a), and the extracted form error, obtained by directly comparing the desired and estimated surface in the same coordinate system, is shown in Fig. 7(b). As shown in Fig. 7(a), the hexagonal lenslets appear to have distortion with a counter-clockwise angle γ, which might be caused by the phase-lag effects of the tool motion, as illustrated in Fig. 2(b).

With respect to the central lenslet, there is no form error due to its rotational symmetry, as observed in Fig. 7(b). As the distance from the lenslet to the rotational centre increases, the form error gradually increases symmetrically around the spindle axis. This result is reasonable because the desired command for the outer lenslets may consist of components with higher frequencies, which will lead to larger tracking errors, as shown in Fig. 2(b). Compared with the results reported in [5], the overall distribution of the estimated form error shows good agreement with that obtained experimentally, where the MLA was turned with another ultra-precision machine tool (250UPL, Moore Nanotech, USA).

The height distribution of the form error for each lenslet also appears to be non-uniform, as shown in Fig. 7(b). Because of the phase-lag between the desired command and the tool motion, a negative form deviation is observed where the tool exits (A_1), while a positive deviation occurs where the tool enters (A_2). The frequency-dependent amplitude variation may further deteriorate the non-uniform form error. Moreover, a bulge-like form deviation is observed where the tool enters (A_2) for each lenslet, and this deviation is more severe for lenslets further from the rotational centre. Relative to the tool motion in the time domain, this bulge-like deviation is primarily induced by the resonant vibration that occurs at sharp points, as illustrated in Fig. 5.

Note 4. Considering the relationship between position and cutting velocity, the frequency of the tool motion may vary with respect to its radial position in the STS turning of complex-shaped surfaces. Therefore, the frequency-dependent, phase-lag-induced surface distortion measured by angle γ may vary with respect to the cutting position.

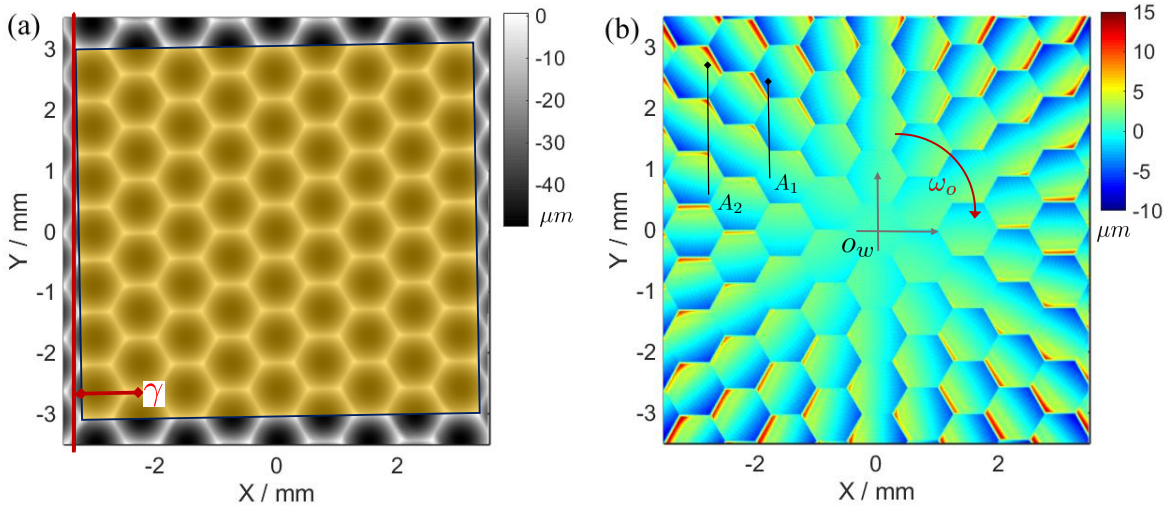

Figure 7: The numerically simulated surface. (a) The projected topography of the generated surface, and (b) the extracted form error, where o_w is the rotational center, and the red arrow denotes the spindle rotation direction.

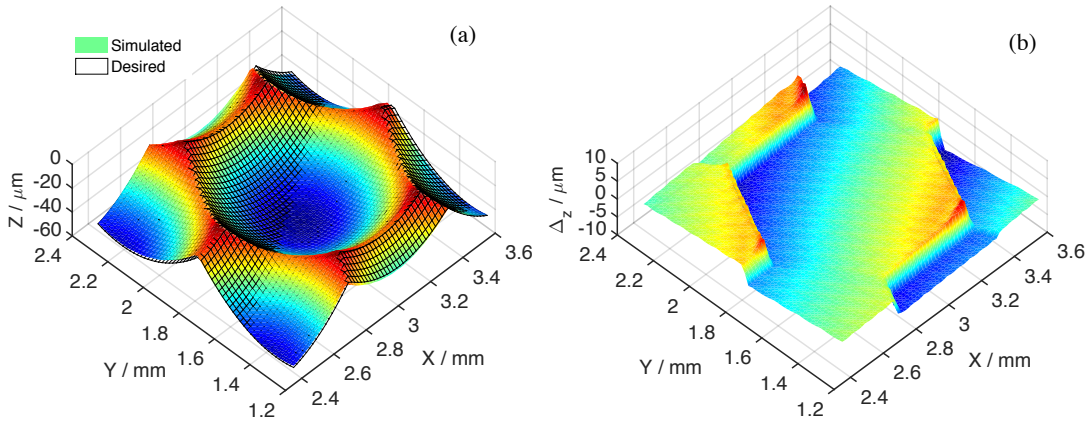

Figure 8: Regional characterization of the simulated surface. (a) The 3D topography of the generated surface, and (b) the deviation between the desired and simulated surfaces.

4.3.2. Velocity-dependent effect

To better characterise the generated surfaces and compare the form errors at different spindle speeds, another simulation is conducted using a spindle speed of $n = 15$ rpm. The simulated and desired surfaces of one lenslet with X-axial coordinates from 2.3 mm to 3.5 mm and Y-axial coordinates from 1.2 mm to 2.4 mm are shown in Fig. 8(a). Overall, a slight position shift superimposed with a surface inclination is observed between the desired and estimated lenslets.

After subtracting the desired surface from the simulated surface, the extracted form error is illustrated in Fig. 8(b). The error distribution is similar to that shown in Fig. 7(b), with an obvious inclination and having step-like features at the connection edges. Moreover, the generated form errors (PV) at spindle speeds of 30 rpm and 15 rpm are approximately 18.7 μm and 11 μm, respectively. Recall that the trajectory tracking errors are approximately 16.5 μm and 7.6 μm for the two cases. The form errors are much larger than the trajectory tracking errors, suggesting that the relationship between servo dynamics errors and form errors is stronger. Therefore, to generate a surface with an acceptable form error, slower spindle speed is required to obtain a smaller tracking error.

5. CTS for dynamic error compensation

As discussed in section 4, the servo dynamics errors of an STS system may lead to overly large form errors. Considering the stroke required for the turning, it is difficult to improve the dynamic performance of the servo axis of an STS. Inspired by the dual-stage positioning system that adopts a fine stage to compensate for the motion error of the coarse stage [33, 34], the proposed CTS system adopts a cooperative operation between an STS and an FTS to overcome the inherent dynamic limitations of the STS.

Unlike what happens in dual-stage positioning systems, both the STS and FTS are 'fine stages' with ultra-high positioning accuracy, and the CTS tries to employ a faster stage (FTS) to compensate for a slower stage (STS) to break through the high-frequency tracking performance limitation of the STS. In addition, although the FTS has been widely employed for error compensation, it has been primarily applied to correct static geometric errors of machine tools [35, 36]. With respect to the CTS, the FTS is applied to cooperatively operate with the STS to compensate for the servo dynamics errors in real-time.

5.1. Principle of the CTS

A schematic diagram of the principle of the CTS is shown in Fig. 9. Since we cannot obtain commands from the control systems of commercial machine tools, a spline-based interpolation is adopted to estimate a command using the measured spindle position and the calculated toolpath. Accordingly, the dynamic error $e_s(t)$ is obtained by directly comparing the measured tool motion and the estimated command of the STS; namely, $e_s(t) = z_d(t) - z_s(t)$. Taking the error $e_s(t)$ as the desired reference for the FTS, the master-slave control strategy is constructed for the cooperative control of the diamond tool.

Without loss of generality, the dynamics of the closed-loop FTS is equivalent to a spring-mass-damping system with unit static gain, and the transfer function relating its desired command and practical motion can be expressed by

$$G_p(s) = \frac{Z_f(s)}{E_s(s)} = \frac{\omega_p^2}{s^2 + 2\xi_p\omega_p s + \omega_p^2}, \tag{15}$$

where $Z_f(s) = \mathcal{L}[z_f(t)]$ denotes the practical motion of the FTS, and $E_s(s) := \mathcal{L}[e_s(t)] = Z_d(s) - Z_s(s)$.

Following the principle shown in Fig. 9, the tool motion of the CTS can be derived by ignoring the dynamic coupling between the FTS and STS system as follows:

$$Z_c(s) = Z_f(s) + Z_s(s) = [Z_d(s) - Z_s(s)]\, G_p(s) + Z_s(s). \tag{16}$$

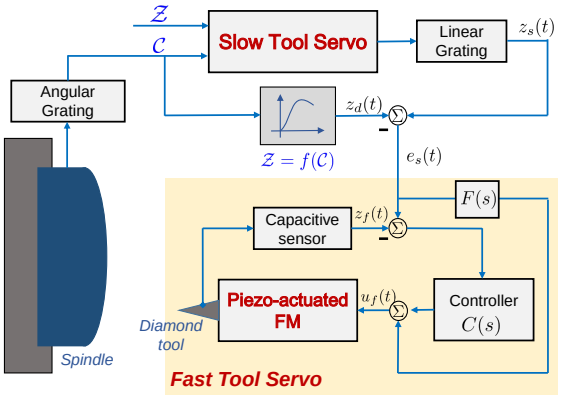

Figure 9: Principle of the proposed CTS diamond turning, where $\mathcal{Z}$ is the Z-axis coordinate of the CLP for a specified surface, and it is directly related to the spindle rotation angle $\mathcal{C}$ using an interpolation function $f(\cdot)$; namely, $\mathcal{Z} = f(\mathcal{C})$.

Therefore, the overall tracking error for the CTS yields

$$E_c(s) = Z_d(s) - Z_c(s) = [1 - G_p(s)]\, E_s(s). \tag{17}$$

With respect to a specified working frequency ω, the amplitude of the tracking error of the CTS can be expressed in the frequency domain as

$$|E_c(j\omega)| = \left| \frac{\left(\frac{\omega}{\omega_p}\right)^2 + 2\xi_p \left(\frac{\omega}{\omega_p}\right) j}{-\left(\frac{\omega}{\omega_p}\right)^2 + 2\xi_p \left(\frac{\omega}{\omega_p}\right) j + 1} E_s(j\omega) \right|, \tag{18}$$

In general, the working frequency, including the resonant frequency of the STS, is typically much smaller than the resonant frequency of the closed-loop FTS; namely, $\omega \ll \omega_p$. By ignoring the small second-order $\left(\frac{\omega}{\omega_p}\right)^2$ and multiplying $1 - 2\xi_p \left(\frac{\omega}{\omega_p}\right) j$ with the denominator and numerator of the term $|E_c(j\omega)|$, the amplitude of the final tracking error of the CTS can be obtained as follows:

$$|E_c(j\omega)| \approx \frac{2\xi_p \omega}{\omega_p} |E_s(j\omega)| \ll |E_s(j\omega)|. \tag{19}$$

The relationship in Eq. 19 suggests that the final tool servo motion error will depend on the ratio between the working frequency and resonant frequency of the FTS. With the assumption that $\omega \ll \omega_p$, the resonant vibration and the trajectory tracking error of the STS can be eliminated by adopting the CTS.

Note 5. Because the CTS only works for the measurable error from the slide, the dynamic deformation induced by the slide-tool coupling system k_t cannot be completely compensated by the CTS. In practice, situations in which $k_t \gg k_s$ would allow the CTS to compensate for the dynamic deformation fully.

5.2. Surface generation in the CTS

5.2.1. Surface generation model for the CTS

By combining Eqs. 16 and 3, the free output motion of the CTS related to the desired command can be expressed by

$$Z_c(s) = [1 - G_p(s)]\, G_d(s) Z_d(s) + G_p(s) Z_d(s). \tag{20}$$

Because the working frequency of the STS system is much smaller than the resonant frequency of the FTS, the effect of the cutting force on the deformation of the FTS is assumed to be quasi-static. Therefore, considering the force equilibrium condition, the resulting tool motion of the CTS subjected to an external cutting force can be obtained as follows:

$$Z_{t,c}(s) = Z_c(s) + \left[G_f(s) - k_{pt}^{-1}\right] F_t(s), \tag{21}$$

where k_{pt} denotes the equivalent output stiffness of the closed-loop FTS, which is approximately 10 to 20 times more stiff than that of an open-loop FTS [37].

The cutting force can be obtained as that of the STS by replacing $z_t(t)$ with $z_{t,c}(t) = \mathcal{L}^{-1}[Z_{t,c}(s)]$. The coupled dynamic model is then established by using the MATLAB/Simulink modulus as illustrated in Fig. 10.

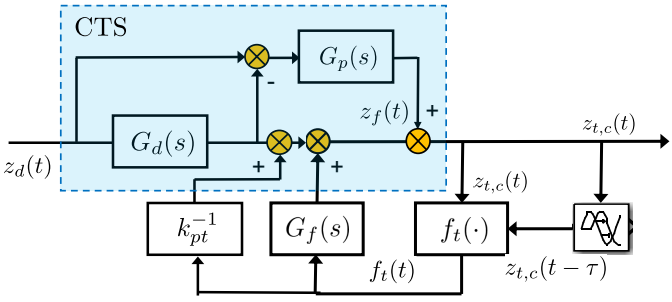

Figure 10: Schematic of the coupled dynamic model for tool motion in CTS.

5.2.2. Simulation results for the CTS

The simulated surface generation for the CTS is obtained using a spindle speed of 15 rpm. The closed-loop output stiffness of the FTS is assumed to be 75 N/μm, which is approximately 15 times its open-loop stiffness, and the equivalent natural frequency and damping ratio of the closed-loop system are assumed to be 1.5 kHz and 0.7, respectively.

The trajectory tracking error $e_c(t)$ illustrated in Fig. 11(a) corresponds to the same segment as that shown in Fig. 5(c). Overall, the tracking error (PV) of the CTS is less than 0.4 μm, which is approximately 5.3% of that of the STS (7.6 μm). It is noteworthy that, as stated in section 4.1, the corresponding tracking error with a spindle speed of 1 rpm is approximately 1 μm, which is much higher than the simulated CTS error with a spindle speed

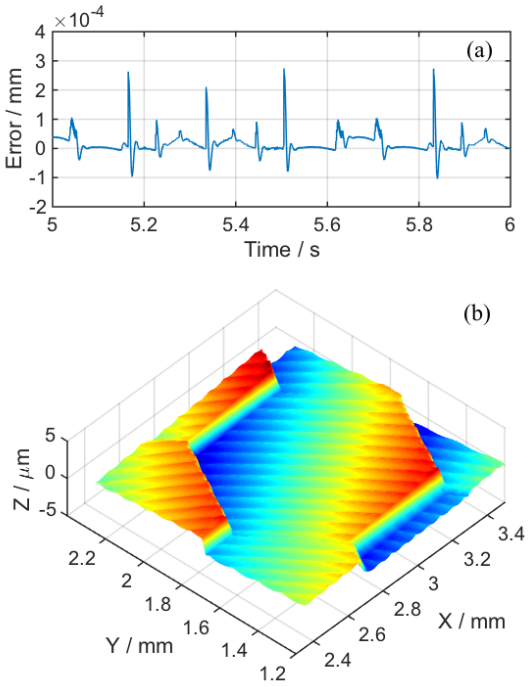

Figure 11: Simulation results of CTS turning. (a) The trajectory tracking error, and (b) the form error.

of 15 rpm. Therefore, these results suggest that manufacturing efficiency could be significantly improved by adopting a CTS when the same tracking accuracy is required.

Furthermore, the estimated deviation of the surface obtained with the CTS is shown in Fig. 11(b). The form error distribution is similar to that obtained with the STS, and the extracted form error (PV) is approximately 4 μm, which is approximately 36% of that obtained with the STS (11.1 μm). This result demonstrates that the proposed cooperative strategy of the CTS improves the generated form accuracy.

6. Experimental results and discussion

6.1. Experimental setup

The turning experiment is shown in Fig. 12. To construct the CTS system, the FTS is independently installed on the closed-loop slide of the STS with its oscillation axis coincident with the servo axis of the STS. With respect to the FTS, a piezo actuator (P-887.51, PI Corporation, Germany) with high dynamics and stiffness is employed to work with a high-performance power amplifier (E617.001, PI Corporation, Germany). A capacitive displacement sensor (gauging module 5810 and probe 5530, MicroSense, USA) is used to measure the practical displacement of the FTS. Assisted by the flexure mechanism, a motion stroke of 18 μm and a natural frequency of approximately 3.2 kHz is obtained. More details about the mechanical design and performance testing of the FTS can be found in [38], and any other FTS system that has a much higher bandwidth

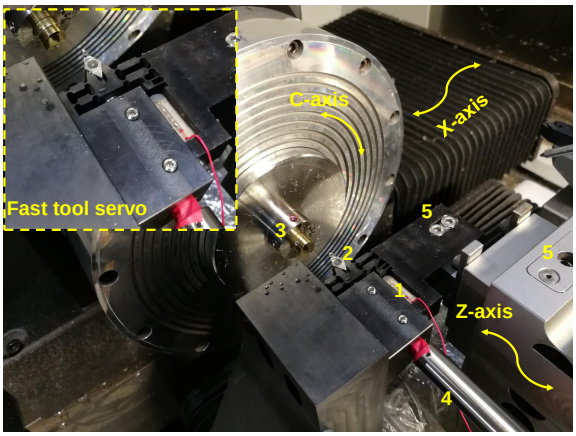

Figure 12: Photograph of the CTS diamond turning system. 1. piezo-actuator; 2. diamond tool; 3. workpiece; 4. capacitive sensor probe; 5. tool holder.

than that of the STS system can be used to construct the CTS.

To construct the feedback control system for the FTS, a simple proportional-integration (PI) controller with a system inversion-based feedforward compensator, as shown in Fig. 9, is employed. Practically, the control system is realised by using a desktop PC running real-time modules in the MATLAB/Simulink environment via a data acquisition board (PCI-6259, NI corporation, USA), and the sampling frequency is set as 20 kHz. The closed-loop resonant frequency of the FTS is more than 1.5 kHz. Considering the low resonant frequency of the STS (53 Hz), the assumption $\omega \ll \omega_p$ is well satisfied to reduce the dynamic error of the CTS significantly.

Table 1: Process parameters for practical turning

Working material	Brass C2600
Sample aperture	10 mm
Feedrate	40 μm
Spindle speed	$\sim$15 rpm
Tool nose radius	1 mm
Rake angle	0
Sampling frequency	20 kHz
FTS stroke	18 μm
FTS closed-loop bandwidth	$>$ 1.5 kHz

The simulated MLA is experimentally turned using the STS and CTS systems. Because the sagitta value of the MLA (50 μm) is much larger than the motion stroke of the FTS, it cannot be independently turned by the FTS. During the turning, a natural single crystal diamond tool (Contour Fine Tooling, UK) is employed with a 1 mm nose radius and a zero rake angle. The spindle speed is automatically determined by the machining system to be approximately 15 rpm, with slight speed fluctuations, and a feedrate of $f_r = 40$ μm/rev is adopted. The machined surface topography is captured by an optical surface profiler (Contour GT-X8, Bruker, USA) with a 20X objective lens, which has a lateral resolution of 0.7 μm. The overall

surface features for one lenslet were obtained by automatically stitching several images. The parameters for the experiment are summarised in Table 1.

6.2. Characteristics of the servo motion

The desired command and practical servo motions of the STS and CTS systems for the turning of an MLA between 5 and 6 s are shown in Fig. 13(a). An enlarged view of the motions between 5.3 and 5.5 s is shown in Fig. 13(b). The STS motion lags behind the desired command, which is attributed to the frequency-dependent phase-lag effects. Moreover, an overly large deviation in the STS motion is induced by the resonant vibration at a position close to the sharp point of the command. In Fig. 13(b), the servo motion of the CTS has much better agreement with the desired command.

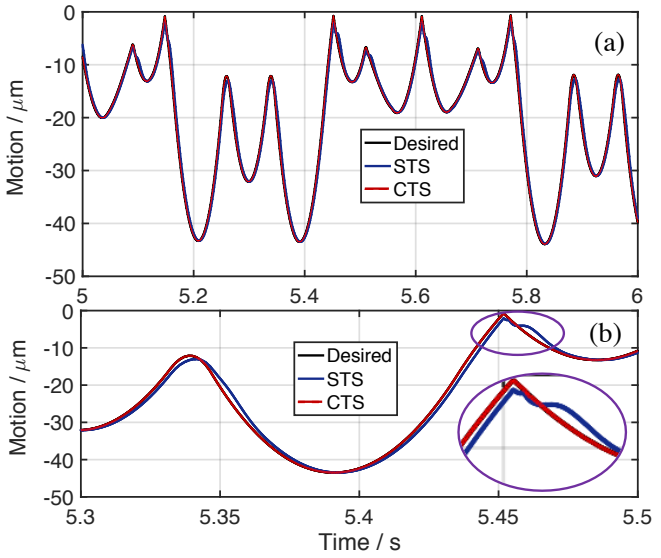

Figure 13: Performance of the tool servo motion. (a) The servo motions of the STS and CTS systems, and (b) an enlarged view.

The servo motion error of the STS ranges from -2.8 μm to 2 μm, as shown in Fig. 14(a). Compared with the numerical simulation shown in Fig. 5(d), the shape of the practical motion error is similar. In addition, as illustrated in Fig. 14(a), the good agreement between the FTS tracking motion and STS error suggests that the FTS is capable of finely tracking the servo motion error of the STS. The overall servo motion error of the CTS system is presented in Fig. 14(b) and exhibits a normal tracking error within $\pm$0.05 μm. The abrupt error induced by the resonant vibration at the sharp point in the command ranges from -0.1 μm to 0.2 μm. This result demonstrates that the CTS decreases the maximum servo motion error (PV) from 5 μm (STS) to 0.3 μm. Compared with the simulated tracking error shown in Fig. 11(a), similar abrupt increases occur at certain positions in practical CTS turning, and the error reduction shows good agreement with that obtained in the simulation.

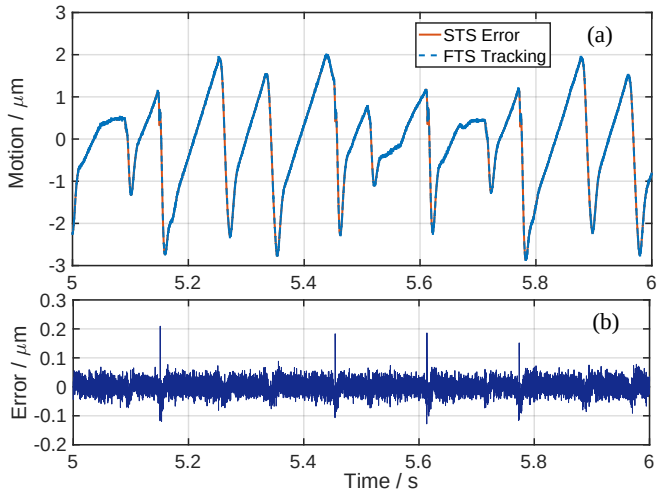

Figure 14: Performance of the cooperative servo motion of the CTS. (a) The tracking motion of the FTS, and (b) the servo motion error of the CTS.

Although the time interval (1 s) is the same as that of the simulation shown in Fig. 5(c), it is noteworthy that the experimental servo motion and the error value is not the same as that obtained in the simulation. This result might be due to the fluctuations in spindle speed that occurred during practical turning.

6.3. Characteristics of the turned surface

The surfaces obtained by turning with the STS and CTS are shown in Figs. 15(a) and 15(c), respectively. These images were captured at a position similar to that used for the simulation shown in Fig. 8. Generally speaking, the surface generated with the CTS has better agreement with the desired target. The form errors generated during practical turning with the STS and CTS are shown in Fig. 15(b) and (d), respectively. These values were obtained by extracting the desired surface with the best fit from the practically obtained surface.

In general, the form errors obtained from turning with the STS and CTS exhibit similar shape features; for example, having steps at the connection edges between the lenslets, and the form error obtained with the STS agrees well with that of the simulation shown in Fig. 8(b). Practically, the form error generated with the STS ranges from -2 μm to 6 μm. The form error generated with the CTS is $\pm$2 μm, which is approximately half that obtained with the STS.

The form error of the hexagonal area of the lenslet is extracted from the hexagonal form errors generated by practical turning with the STS and CTS by recalculating the simulated surface of the central hexagonal region with the best fit. These results are shown in Figs. 16(a) and (b), respectively. Overall, an abrupt form error caused by the resonant vibration is observed for the surface generated with the STS, and the form error of the surface generated with the CTS appears much smoother.

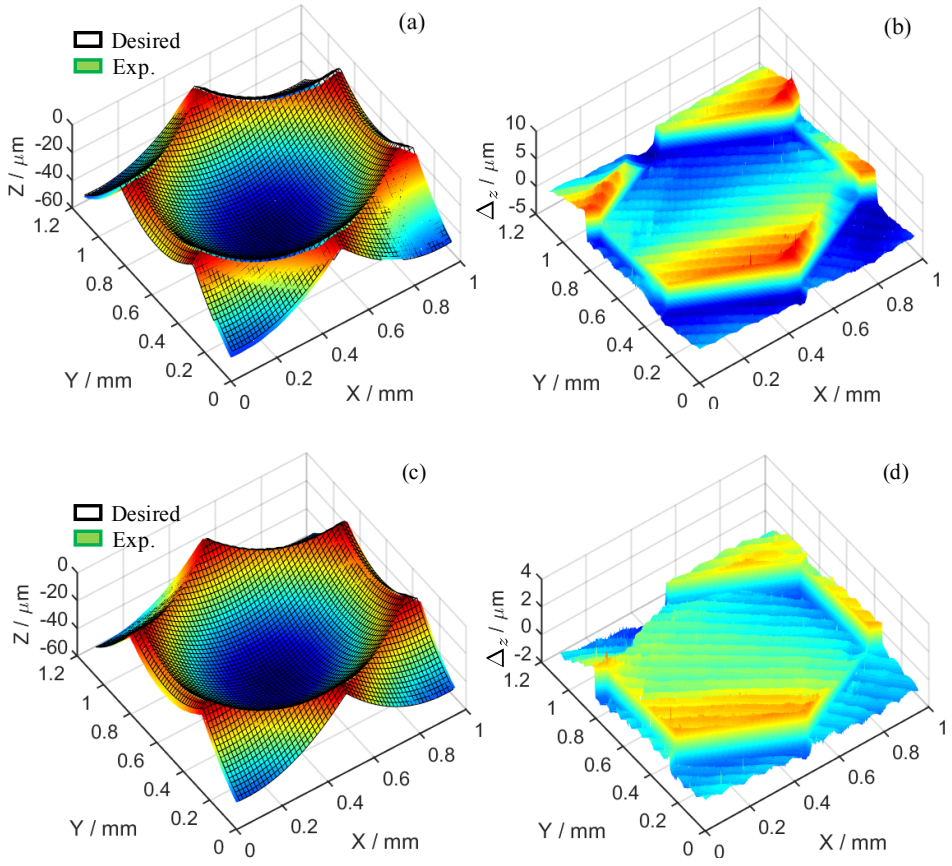

Figure 15: Characteristics of the surfaces obtained by practical turning. (a) The 3D profile and (b) the resulting form error of the surface generated by STS turning. (c) The 3D profile and (d) the resulting form error of the surface generated by CTS turning.

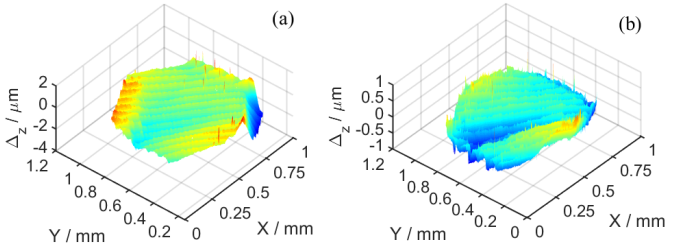

Figure 16: Form error of one hexagonal lenslet generated by practical turning with (a) the STS, and (b) the CTS.

Statistically, the PV form error generated by turning with the STS is approximately 4 μm, while that for the CTS is approximately 1.4 μm, which is approximately 35% of that obtained with the STS. These results suggest that the CTS improves the form accuracy by compensating for the servo dynamics errors. Both the simulated and experimental results obtained by turning with STS and CTS are summarised in Table 2. Overall, the results and the tendencies for error evolution obtained in the simulations have good agreement with the experimental results.

Table 2: Summary of results for STS and CTS turning

	STS		CTS	
	Simul.	Exp.	Simul.	Exp.
Spindle speed n / rpm	30	15	∼15	15	∼15
Tracking error / μm	16.5	7.6	4.8	0.4	0.3
Form error / μm	18.7	11.1	8.0	4.0	4.0
Form error (H) / μm	—	—	4.0	—	1.4

Note: 'H' means the hexagonal region.

7. Conclusion

The effects of servo dynamics errors on the form accuracy were investigated for slow tool servo diamond turning of complex-shaped optics, and a real-time compensation strategy was proposed to enhance the form accuracy. The main conclusions of this paper are drawn as follows:

- In addition to the reported geometric error, the servo dynamics errors were identified in this paper as dominant error sources for the surface generation in slow tool servo diamond turning. A dynamic surface generation model was proposed, which enables the prediction of the tool motion error as well as the generated form error. The model was validated by practically turning a spherical micro-lens array.

- Further, this paper proposed a new cooperative tool servo turning strategy. Through adopting a master-slave control strategy, a fast tool servo was incorporated into the slow tool servo to compensate for its servo dynamics errors in real-time. The cooperative concept was demonstrated both analytically and numerically.
- By turning a micro-lens array through the cooperative tool servo, the peak-to-valley (P-V) trajectory tracking error reaches 0.3 μm and the form accuracy achieves 1.4 μm (P-V), compared with the motion error of 4.8 μm (P-V) and form error of 4 μm obtained by slow tool servo.

Appendix A. Tool motion mapping

Without loss of generality, a strategy of constant angle sampling and constant side-feeding is adopted for determining the toolpath for STS turning. With the l-th CLP $o_{k,l}$ in the k-th revolution, the radial and angular positions of the tool path can be expressed by

$$\begin{cases} \rho_{k,l} = \rho_o - (k+\alpha)\, f_r \\ \theta_{k,l} = 2\pi\,(k+\alpha) \end{cases} \tag{A.1}$$

where $\alpha = \frac{l}{N}$, with N denoting the sampling number for each revolution, and f_r is the feedrate per revolution.

Using the angular position as a reference, the required $z-$axial tool position $z_{k,l}$ can be obtained accurately in the coordinate system of the machine tool by identifying the minimum approaching distance between the edge of the cutter and the desired surface [29].

Taking advantage of the inherent relationship between the spindle angle $\theta_{k,l}$ and the z-axial position $z_{k,l}$, the required tool servo motion can be mapped into the time domain as $z_d(t)$ by setting the time $t := t_{k,l}$ as

$$t = \frac{30\theta_{k,l}}{n\pi} = \frac{60\,(kN+l)}{nN}, \tag{A.2}$$

where n the denotes the spindle speed, which is assumed to be constant in the simulation.

Appendix B. Effective material removal area

The engagement between the tool and work material at the CLP $o_{k,l}$ is illustrated in Fig. B.17, and $o-xz$ is defined as the local coordinate system, where the oz-axis passes through the point $o_{k,l}$. In this system, the coordinate of a point A that interacts with the tool edges at CLPs $o_{k-1,l}$ and $o_{k,l}$ can be expressed by

$$\begin{cases} x_a = -f_r - d_a \\ z_a = z_{k-1,l} - \sqrt{r_\epsilon^2 - d_a^2} \end{cases} \tag{B.1}$$

where $d_a = \left|\overrightarrow{AA_p}\right|$ is the distance from point A to the vertical line passing through $o_{k-1,l}$. From the geometric relationship in $\triangle O_{k-1,l}AA_p$, the distance d_a is

$$d_a = \frac{z_{k-1,l} - z_{k,l}}{f_r} r_\epsilon - \frac{f_r}{2}, \tag{B.2}$$

where r_ϵ denotes the tool nose radius.

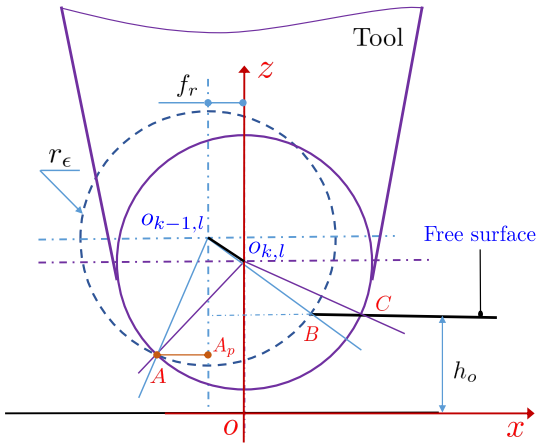

Figure B.17: Schematic of material removal for the l-th cutting point in the k-th revolution.

Assume that the free surface is planar and the nominal depth-of-cut is h_o; the z-axial coordinates for points B and C are $z_b = z_c = h_o$. Furthermore, the corresponding x-axial coordinates are

$$\begin{cases} x_b = \sqrt{r_\epsilon^2 - (z_{k-1,l} - h_o)^2} - f_r \\ x_c = \sqrt{r_\epsilon^2 - (z_{k,l} - h_o)^2} \end{cases} \tag{B.3}$$

Therefore, the areas S_1 and S_2 for the two sector regions $\widehat{O_{k,l}AC}$ and $\widehat{O_{k-1,l}AB}$ can be expressed by

$$S_1 = \frac{\theta_{AC}}{2} r_\epsilon^2 = r_\epsilon^2 \cdot \arcsin\frac{|P_c - P_a|}{2r_\epsilon}, \tag{B.4}$$

$$S_2 = \frac{\theta_{AB}}{2} r_\epsilon^2 = r_\epsilon^2 \cdot \arcsin\frac{|P_b - P_a|}{2r_\epsilon}, \tag{B.5}$$

where $P_a = (x_a, y_a)$, $P_b = (x_b, y_b)$, and $P_c = (x_c, y_c)$.

The area of $\triangle O_{k-1,l}O_{k,l}A$ can be obtained as

$$\begin{cases} S_3 = \sqrt{\frac{L_0}{2}\left(\frac{L_0}{2} - a_0\right)\left(\frac{L_0}{2} - b_0\right)\left(\frac{L_0}{2} - c_0\right)} \\ a_0 = b_0 = r_\epsilon, c_0 = \sqrt{(z_{k-1,l} - z_{k,l})^2 + f_r^2} \end{cases} \tag{B.6}$$

where $L_0 = a_0 + b_0 + c_0$ is the perimeter of $\triangle O_{k-1,l}O_{k,l}A$.

The area of the quadrilateral $O_{k-1,l}O_{k,l}CB$ can be calculated as a sum of the areas of $\triangle O_{k-1,l}O_{k,l}B$ and $\triangle O_{k,l}CB$, which can be derived as

$$S_4 = \sum_{i=1}^{2} \sqrt{\frac{L_i}{2}\left(\frac{L_i}{2} - a_i\right)\left(\frac{L_i}{2} - b_i\right)\left(\frac{L_i}{2} - c_i\right)}, \tag{B.7}$$

where $a_1 = a_2 = r_\epsilon$, $c_1 = c_0$, $c_2 = x_c - x_b$, and $b_1 = b_2 = |P_{k,l} - P_b|$. L_1 and L_2 are the perimeters of $\triangle O_{k-1,l} O_{k,l} B$ and $\triangle O_{k,l} CB$, respectively.

Finally, the effective material removal area can be obtained as

$$S_c = S_1 + S_3 - S_2 - S_4. \tag{B.8}$$

Reference

References

[1] F. Fang, X. Zhang, A. Weckenmann, G. Zhang, C. Evans, Manufacturing and measurement of freeform optics, CIRP Annals 62 (2) (2013) 823–846.

[2] X. Liu, X. Zhang, F. Fang, S. Liu, Identification and compensation of main machining errors on surface form accuracy in ultra-precision diamond turning, International Journal of Machine Tools and Manufacture 105 (2016) 45–57.

[3] D. P. Yu, G. S. Hong, Y. San Wong, Profile error compensation in fast tool servo diamond turning of micro-structured surfaces, International Journal of Machine Tools and Manufacture 52 (1) (2012) 13–23.

[4] L. Kong, C. Cheung, T. Kwok, Theoretical and experimental analysis of the effect of error motions on surface generation in fast tool servo machining, Precision Engineering 38 (2) (2014) 428–438.

[5] X. Liu, X. Zhang, F. Fang, Z. Zeng, H. Gao, X. Hu, Influence of machining errors on form errors of microlens arrays in ultra-precision turning, International Journal of Machine Tools and Manufacture 96 (2015) 80–93.

[6] F. Fang, X. Zhang, X. Hu, Cylindrical coordinate machining of optical freeform surfaces, Optics Express 16 (10) (2008) 7323–7329.

[7] Z. Zhu, S. To, Adaptive tool servo diamond turning for enhancing machining efficiency and surface quality of freeform optics, Optics express 23 (16) (2015) 20234–20248.

[8] K. Nagayama, J. Yan, A comprehensive error correction/prediction system for tool-servo driven diamond turning of freeform surfaces, in: European Society for Precision Engineering and Nanotechnology, Conference Proceedings - 18th International Conference and Exhibition, EUSPEN 2018, euspen, 2018, pp. 51–52.

[9] H.-S. Kim, K.-I. Lee, K.-M. Lee, Y.-B. Bang, Fabrication of freeform surfaces using a long-stroke fast tool servo and corrective figuring with on-machine measurement, International Journal of Machine Tools and Manufacture 49 (12) (2009) 991 – 997.

[10] D. Li, B. Wang, Z. Qiao, X. Jiang, Ultraprecision machining of microlens arrays with integrated on-machine surface metrology, Opt. Express 27 (1) (2019) 212–224.

[11] X. Zhang, Z. Zeng, X. Liu, F. Fang, Compensation strategy for machining optical freeform surfaces by the combined on- and off-machine measurement, Opt. Express 23 (19) (2015) 24800–24810.

[12] Z. Zhu, S. To, S. Zhang, Large-scale fabrication of micro-lens array by novel end-fly-cutting-servo diamond machining, Opt. Express 23 (16) (2015) 20593–20604.

[13] Y. Liu, Z. Qiao, D. Qu, Y. Wu, J. Xue, D. Li, B. Wang, Experimental investigation on form error for slow tool servo diamond turning of micro lens arrays on the roller mold, Materials 11 (10).

[14] Z. Zhu, S. To, W.-L. Zhu, P. Huang, Feasibility study of the novel quasi-elliptical tool servo for vibration suppression in the turning of micro-lens arrays, International Journal of Machine Tools and Manufacture 122 (2017) 98 – 105.

[15] L. Zhang, N. J. Naples, W. Zhou, A. Y. Yi, Fabrication of infrared hexagonal microlens array by novel diamond turning method and precision glass molding, Journal of Micromechanics and Microengineering 29 (6) (2019) 065004.

[16] M. Mukaida, J. Yan, Fabrication of hexagonal microlens arrays on single-crystal silicon using the tool-servo driven segment turning method, Micromachines 8 (11).

[17] Adaptive control technology, `https://www.precitech.com/product/accessoriesoverview/adaptivecontroltechnology`, accessed February 15, 2020.

[18] W.-L. Zhu, X. Yang, F. Duan, Z. Zhu, B.-F. Ju, Design and adaptive terminal sliding mode control of a fast tool servo system for diamond machining of freeform surfaces, IEEE Transactions On Industrial Electronics 66 (6) (2019) 4912–4922.

[19] D. Wu, K. Chen, X. Wang, Tracking control and active disturbance rejection with application to noncircular machining, International Journal of Machine Tools and Manufacture 47 (15) (2007) 2207–2217.

[20] M. F. Byl, S. J. Ludwick, D. L. Trumper, A loop shaping perspective for tuning controllers with adaptive feedforward cancellation, Precision Engineering 29 (1) (2005) 27–40.

[21] W. Lee, C. Cheung, A dynamic surface topography model for the prediction of nano-surface generation in ultra-precision machining, International Journal of Mechanical Sciences 43 (4) (2001) 961–991.

[22] X. Luo, K. Cheng, R. Ward, The effects of machining process variables and tooling characterisation on the surface generation, The International Journal of Advanced Manufacturing Technology 25 (11-12) (2005) 1089–1097.

[23] L. Zhou, K. Cheng, Dynamic cutting process modelling and its impact on the generation of surface topography and texture in nano/micro cutting, Proceedings of the Institution of Mechanical Engineers, Part B: Journal of Engineering Manufacture 223 (3) (2009) 247–266.

[24] Y. Altintas, A. Verl, C. Brecher, L. Uriarte, G. Pritschow, Machine tool feed drives, CIRP annals 60 (2) (2011) 779–796.

[25] C. He, W. Zong, J. Zhang, Influencing factors and theoretical modeling methods of surface roughness in turning process: State-of-the-art, International Journal of Machine Tools and Manufacture 129 (2018) 15–26.

[26] Z. Niu, F. Jiao, K. Cheng, Investigation on innovative dynamic cutting force modelling in micro-milling and its experimental validation, Nanomanufacturing and Metrology 1 (2) (2018) 82–95.

[27] Z.-L. Li, O. Tuysuz, L.-M. Zhu, Y. Altintas, Surface form error prediction in five-axis flank milling of thin-walled parts, International Journal of Machine Tools and Manufacture 128 (2018) 21–32.

[28] Z. Kilic, Y. Altintas, Generalized mechanics and dynamics of metal cutting operations for unified simulations, International Journal of Machine Tools and Manufacture 104 (2016) 1–13.

[29] Z. Zhu, S. To, W.-L. Zhu, P. Huang, X. Zhou, Cutting forces in fast-/slow tool servo diamond turning of micro-structured surfaces, International Journal of Machine Tools and Manufacture 136 (2019) 62–75.

[30] W.-L. Zhu, F. Duan, X. Zhang, Z. Zhu, B.-F. Ju, A new diamond machining approach for extendable fabrication of micro-freeform lens array, International Journal of Machine Tools and Manufacture 124 (2018) 134–148.

[31] O. Gonzalo, J. Beristain, H. Jauregi, C. Sanz, A method for the identification of the specific force coefficients for mechanistic milling simulation, International Journal of Machine Tools and Manufacture 50 (9) (2010) 765–774.

[32] J. Gradišek, M. Kalveram, K. Weinert, Mechanistic identification of specific force coefficients for a general end mill, International Journal of Machine Tools and Manufacture 44 (4) (2004) 401–414.

[33] C.-W. Chen, Y.-C. Chang, T.-C. Tsao, Dynamic trajectory tracking by synergistic dual-stage actuation and control, IEEE/ASME Transactions on Mechatronics 22 (6) (2017) 2600–2610.

[34] A. Elfizy, G. Bone, M. Elbestawi, Design and control of a dual-stage feed drive, International Journal of Machine Tools and Manufacture 45 (2) (2005) 153–165.

[35] W. Gao, M. Tano, T. Araki, S. Kiyono, C. H. Park, Measure-

ment and compensation of error motions of a diamond turning machine, Precision Engineering 31 (3) (2007) 310–316.
[36] S.-W. Gan, L. Han-Seok, M. Rahman, F. Watt, A fine tool servo system for global position error compensation for a miniature ultra-precision lathe, International Journal of Machine Tools and Manufacture 47 (7-8) (2007) 1302–1310.
[37] Y. Tian, B. Shirinzadeh, D. Zhang, A flexure-based mechanism and control methodology for ultra-precision turning operation, Precision Engineering 33 (2) (2009) 160–166.
[38] Z. Zhu, L. Chen, P. Huang, L. Schönemann, O. Riemer, J. Yao, S. To, W.-L. Zhu, Design and control of a piezoelectrically actuated fast tool servo for diamond turning of micro-structured surfaces, IEEE Transactions on Industrial Electronics (2019) doi: 10.1109/TIE.2019.2937051.